Simulating photon-transport in uniform media using the radiative transport equation: a study using the Neumann-series approach

Abhinav K. Jha,[1],* Matthew A. Kupinski,[1],[2] Takahiro Masumura,[3] Eric Clarkson,[1],[2] Alexey V. Maslov,[3] and Harrison H. Barrett[1],[2]

[1]*College of Optical Sciences, University of Arizona, Tucson, Arizona, USA*
[2]*Department of Radiology, University of Arizona, Tucson, Arizona, USA*
[3]*Optics Research Laboratory, Canon USA Inc., Tucson, Arizona, USA*
*Corresponding author: akjha@email.arizona.edu

We present the implementation, validation, and performance of a Neumann-series approach for simulating light propagation at optical wavelengths in uniform media using the radiative transport equation (RTE). The RTE is solved for an anisotropic-scattering medium in a spherical harmonic basis for a diffuse-optical-imaging setup. The main objectives of this paper are threefold: to present the theory behind the Neumann-series form for the RTE, to design and develop the mathematical methods and the software to implement the Neumann series for a diffuse-optical-imaging setup, and, finally, to perform an exhaustive study of the accuracy, practical limitations, and computational efficiency of the Neumann-series method. Through our results, we demonstrate that the Neumann-series approach can be used to model light propagation in uniform media with small geometries at optical wavelengths.   © 2012 Optical Society of America

OCIS codes: 170.3660, 000.3860, 110.2990.

1. INTRODUCTION

With the development of many optical imaging modalities, simulating light propagation in tissue at optical wavelengths has gained increasing importance as a research problem. Various optical imaging modalities such as diffuse optical tomography (DOT) [1–3], optical fluorescence imaging [4], fluorescence tomography [5], optical coherence tomography [6], and oblique incidence reflectometry [7] require modeling of light transfer in biological tissue at optical wavelengths. The radiative transport equation (RTE) is a well-known method for modeling this light propagation [8]. However, the RTE is a computationally intensive integro-differential equation. Therefore, research is being pursued to develop computationally efficient and accurate methods to solve the RTE.

In order to reduce the computational complexity of the RTE, an approximation to this equation, known as the diffusion approximation, is commonly used. The diffusion approximation has been implemented with finite element methods [9–12] and boundary element methods [13,14]. This approximation assumes that light propagates diffusely in tissues. However, this assumption breaks down near tissue surface, in anisotropic tissues, and in regions of high absorption or low scatter [1,3,15,16]. Consequently, the diffusion approximation cannot accurately describe light propagation in highly absorbing regions such as haematomas, and voidlike spaces such as ventricles and the subarachnoid-space [16–20]. The diffusion model is also not accurate when imaging small tissue geometries, e.g., whole-body imaging of small animals 15.

To overcome these issues, higher-order approximations to the RTE such as the discrete ordinates method (S_N) [21] and spherical harmonic equations (P_N) [22,23] have been developed. The discrete ordinates method has been implemented with finite difference [16,19,24] and boundary element [25] methods. Also, the spherical harmonics method has been used along with finite element methods [26,27]. These approximations lead to exact solutions as $N \to \infty$. However, the number of P_N equations grows as $(N + 1)^2$ for a three-dimensional (3D) medium, where N is the number of Legendre polynomials. Similarly, the S_N method, which uses discrete ordinates, solves a system of $N(N + 2)$ coupled equations [15]. Therefore, these methods are still computationally expensive. To illustrate their computational requirement, a full 3D image reconstruction of the mouse model for recovering the fluorescent-probe-distribution can take up to several hours or days of computation time using these methods [15]. To improve the computational efficiency, a simplified spherical harmonics (SP_N) approximation has been validated [15,20]. Although the method is asymptotic, it can model light propagation with small error, and is computationally less expensive.

While there has thus been significant research on using the RTE to model light propagation in biological tissue for optical imaging, these approaches have mostly focused on differential methods to solve the RTE. The differential methods require solutions to many coupled differential equations to determine the RTE solution. Conversely, in nuclear imaging, it is common to use approximations of the integral form of the RTE to model photon propagation [28–30]. The advantage with integral-based methods is that, unlike the differential methods, they do not require solutions to many coupled equations. However, in nuclear imaging, photon propagation occurs in the forward direction, and scattering effects are minimal.

Therefore, using integral methods is more convenient in nuclear imaging than in optical imaging, where scattering effects are dominant. However, even in optical imaging, the scattering phenomenon is strongly forward-biased [15,31–33]. Therefore, it was of interest for us to study the validity and performance of the integral form of the RTE, using a Neumann-series formulation, for an optical imaging modality.

This paper is an outcome of this study, where we develop the Neumann-series form of the RTE for optical imaging applications, and then test its performance exhaustively for different kinds of media. While the framework that we propose is general, each imaging modality has certain details specific to itself. Therefore, in this study, we focus on implementing and testing the Neumann-series RTE for one particular imaging modality: DOT.

DOT has attracted significant attention over the past decade as a noninvasive biomedical-imaging technique. The goal in DOT is to probe the tissue with near-infrared (NIR) light to determine its absorption and scattering properties [1–3,34]. These absorption and scattering properties can be used by physicians to determine the absence or presence of various diseases. For example, the absorption varies greatly between water, deoxygenated-hemoglobin, and oxygenated-hemoglobin [2]. DOT can also be used in breast-imaging applications to study areas of increased vascularization that are indicative of cancer. This imaging modality has been applied in breast-cancer detection and characterization [35,36], in functional brain imaging [37,38], in imaging of small joints for early diagnosis of rheumatoid arthritis [39] and in small-animal imaging for studying physiological processes and pathologies [40]. However, DOT is a model-based imaging modality, which implies that to perform the task of image reconstruction, the DOT system should be modeled accurately. An important part of modeling the DOT system is to simulate light propagation through biological tissue accurately. Therefore, we are interested in investigating the accuracy and performance of the Neumann-series form of the RTE for this task.

The Neumann-series formulation of the RTE has been explored for various other tasks that require simulating photon propagation, such as modeling scattering effects in nuclear imaging [28,41,42], retrieving atmospheric properties from remotely sensed microwave observations [43], modeling the scatter of sun light in the atmosphere [44], and solving neutron-transport equations [45]. However, in optical imaging, the scattering function, emission source, geometry of the experimental setup, and some other factors are very different from the above cases. In this paper, our first objective is to present the Neumann-series solution of the RTE and extend it to model light propagation at optical wavelengths. Our second goal is to develop the mathematical methods and the software to implement the Neumann series for a DOT setup. However, the most important objective of this paper is to study the performance of the Neumann-series solution of the RTE for optical imaging. We validate whether the Neumann-series form for the RTE can be used to model light propagation in tissue at optical wavelengths. The convergence characteristics of the developed algorithm are also studied. We investigate the practical limitations and the computational requirements of the implementation. Since this is one of the first studies in this direction, for the purposes of simplicity, we assume that the medium through which light propagation

occurs is homogeneous. This assumption helps to simplify the computational task considerably, as we elaborate on in the later sections. We begin with introducing the theory of the Neumann-series form of the RTE.

2. THEORY

The RTE, also known as the Boltzmann's equation, describes the spatio-temporal propagation of photons through a medium. Before introducing the RTE, we describe some of the radiometric quantities that are important to represent the equation. The fundamental radiometric quantity that we describe using the RTE is the distribution function $w(\mathbf{r}, \hat{s}, \mathcal{E}, t)$. In terms of photons, $w(\mathbf{r}, \hat{s}, \mathcal{E}, t)\Delta V \Delta \Omega \Delta \mathcal{E}$ can be interpreted as the number of photons contained in volume ΔV centered on the 3D vector $\mathbf{r}$, traveling in solid angle $\Delta \Omega$ about direction $\hat{s}$, and having energies between $\mathcal{E}$ and $\mathcal{E} + \Delta \mathcal{E}$ at time t. The distribution function is a complete characterization of the position, direction, and energy of the photons in a medium as a function of time. Another important radiometric quantity is the source function $\Xi(\mathbf{r}, \hat{s}, \mathcal{E}, t)$, which describes the injection of photons into a medium. Like the distribution function, $\Xi(\mathbf{r}, \hat{s}, \mathcal{E}, t)\Delta V \Delta \Omega \Delta \mathcal{E}$ can be interpreted as the number of photons injected per second into volume ΔV in energy range $\Delta \mathcal{E}$, over solid angle $\Delta \Omega$, and at time t.

For the diffuse-optical-imaging implementation, we assume a monoenergetic emission source. Thus, the source function can be written without any dependence on energy as $\Xi(\mathbf{r}, \hat{s}, t)$. In addition, in optical imaging, the dominant scattering mechanism is elastic scattering. This assumption implies that a scattered photon does not lose any energy. Since there are no energy-loss mechanisms for the photons, the dependence on energy in the distribution function can be dropped completely, which allows us to write the distribution function as $w(\mathbf{r}, \hat{s}, t)$.

A. RTE
The RTE is an equation for the time-derivative of $w(\mathbf{r}, \hat{s}, t)$, or w for short, and is given, very generally, as [8]

$$\frac{dw}{dt} = \left[\frac{\partial w}{\partial t}\right]_{\text{abs}} + \left[\frac{\partial w}{\partial t}\right]_{\text{em}} + \left[\frac{\partial w}{\partial t}\right]_{\text{prop}} + \left[\frac{\partial w}{\partial t}\right]_{\text{sc}}. \qquad (1)$$

In the above equation, the time-derivative of the distribution function has contributions from absorption, emission, propagation, and scatter, respectively. We now examine each of these terms in detail.

We can describe the time-derivative of the distribution function due to absorption as [8]

$$\left[\frac{\partial w}{\partial t}\right]_{\text{abs}} = -c_{\text{m}}\mu_a(\mathbf{r})w(\mathbf{r}, \hat{s}, t), \qquad (2)$$

where $\mu_a(\mathbf{r})$ is the absorption coefficient of the medium as a function of position and c_{m} is the speed of light in the medium. In this study, we assume that the speed of light does not change within the medium.

The emission of light is fully described by the source function, so that

$$\left[\frac{\partial w}{\partial t}\right]_{\text{em}} = \Xi(\mathbf{r}, \hat{s}, t). \qquad (3)$$

The propagation term in Eq. ([1](1)) describes the movement of photons from one location to another and is given by [8]

$$\left[\frac{\partial w}{\partial t}\right]_{\text{prop}} = -c_{\text{m}}\hat{s} \cdot \nabla w(\boldsymbol{r},\hat{s},t). \tag{4}$$

Finally, to describe scattering, we must consider the scattering of photons out of a location and the scattering of photons in from another location. This process is described by [8]

$$\left[\frac{\partial w}{\partial t}\right]_{\text{sc}} = -c_{\text{m}}\mu_s(\boldsymbol{r})w(\boldsymbol{r},\hat{s},t) + \int_{4\pi} \mathrm{d}\Omega' K(\hat{s},\hat{s}'|\boldsymbol{r})w(\boldsymbol{r},\hat{s}',t), \tag{5}$$

where $\mu_s(\boldsymbol{r})$ denotes the scattering coefficient at location $\boldsymbol{r}$. The first term in the above equation describes the photons scattering out of a location, hence the minus sign. The second term describes the scattering of photons from a direction $\hat{s}'$ to the direction $\hat{s}$ at the location $\boldsymbol{r}$. The scattering kernel $K(\hat{s},\hat{s}'|\boldsymbol{r})$ quantifies the probability of this event. The scattering phase function in biological tissue is typically the Henyey–Greenstein function [20,46], so that the scattering kernel is given by

$$K(\hat{s},\hat{s}'|r) = \frac{c_{\text{m}}\mu_s(\boldsymbol{r})}{4\pi}\left\{\frac{1-g^2}{[1+g^2-2g(\hat{s}\cdot\hat{s}')]^{3/2}}\right\}. \tag{6}$$

The anisotropy factor g is used to characterize the angular distribution of the tissue scattering, where for an isotropic medium, $g = 0$. We write the second term in Eq. ([5](5)) in operator notation as $\mathcal{K}w$, so that the effect of the scattering operator on a distribution function is given in general by

$$[\mathcal{K}w](\boldsymbol{r},\hat{s},t) = \int_{4\pi} \mathrm{d}\Omega' K(\hat{s},\hat{s}'|\boldsymbol{r})w(\boldsymbol{r},\hat{s}',t). \tag{7}$$

Collecting together Eqs. ([2](2))–([5](5)) in Eq. ([1](1)),

$$\begin{aligned}\frac{dw}{dt} = &-c_{\text{m}}\mu_{\text{tot}}(\boldsymbol{r})w(\boldsymbol{r},\hat{s},t) + \Xi(\boldsymbol{r},\hat{s},t) \\ &- c_{\text{m}}\hat{s}\cdot\nabla w(\boldsymbol{r},\hat{s},t) + \mathcal{K}w(\boldsymbol{r},\hat{s},t),\end{aligned} \tag{8}$$

where $\mu_{\text{tot}}(\boldsymbol{r}) = \mu_a(\boldsymbol{r}) + \mu_s(\boldsymbol{r})$. We transform Eq. ([8](8)) to the Fourier domain. After rearranging some terms, the equation can be written in the frequency domain at frequency ν as

$$\begin{aligned}\hat{s}\cdot\nabla w(\boldsymbol{r},\hat{s},\nu) &+ \left[\mu_{\text{tot}} + \frac{i\nu}{c_{\text{m}}}\right]w(\boldsymbol{r},\hat{s},\nu) \\ &= \frac{1}{c_{\text{m}}}[\Xi(\boldsymbol{r},\hat{s},\nu) + \mathcal{K}w(\boldsymbol{r},\hat{s},\nu)].\end{aligned} \tag{9}$$

In this paper, we focus on the solution of the RTE for a source that is time-independent, so that the source function, and consequently the distribution function, exist only at $\nu = 0$ frequency. We observe from Eq. ([9](9)) that the implementation of the RTE for a time-independent source can be used easily for a time-dependent source once we replace μ_{tot} with $\mu_{\text{tot}} + \frac{i\nu}{c_{\text{m}}}$. Dropping the dependence on ν in Eq. ([9](9)), we get

$$\hat{s}\cdot\nabla w(\boldsymbol{r},\hat{s}) + \mu_{\text{tot}}w(\boldsymbol{r},\hat{s}) = \frac{1}{c_{\text{m}}}[\Xi(\boldsymbol{r},\hat{s}) + \mathcal{K}w(\boldsymbol{r},\hat{s})]. \tag{10}$$

On integrating Eq. ([10](10)) along $\hat{s}$, we arrive at the integral form of the RTE for a time-independent source

$$\begin{aligned}w(\boldsymbol{r},\hat{s}) = &\frac{1}{c_{\text{m}}}\int_0^\infty \mathrm{d}\Lambda\,\Xi(\boldsymbol{r}-\hat{s}\Lambda,\hat{s})\exp\left[-\int_0^\Lambda \mathrm{d}\Lambda'\mu_{\text{tot}}(\boldsymbol{r}-\hat{s}\Lambda')\right] \\ &+ \frac{1}{c_{\text{m}}}\int_0^\infty \mathrm{d}\Lambda[\mathcal{K}w](\boldsymbol{r} \\ &- \hat{s}\Lambda,\hat{s})\exp\left[-\int_0^\Lambda \mathrm{d}\Lambda'\mu_{\text{tot}}(\boldsymbol{r}-\hat{s}\Lambda')\right].\end{aligned} \tag{11}$$

In operator notation, this is given by

$$w = \mathcal{X}\Xi + \mathcal{X}\mathcal{K}w, \tag{12}$$

where $\mathcal{X}$ is an integral transform, known as the attenuated x-ray transform. This transform describes the propagation of photons interrupted by absorption and out-scatter. We refer to $\mathcal{X}$ as the attenuation operator, and the effect it has on the distribution function is given by

$$[\mathcal{X}w](\boldsymbol{r},\hat{s}) = \frac{1}{c_{\text{m}}}\int_0^\infty \mathrm{d}\Lambda\,w(\boldsymbol{r}-\hat{s}\Lambda,\hat{s})\exp\left[-\int_0^\Lambda \mathrm{d}\Lambda'\mu_{\text{tot}}(\boldsymbol{r}-\hat{s}\Lambda')\right]. \tag{13}$$

After some rearranging, Eq. ([12](12)) can be written as

$$[\mathcal{I} - \mathcal{X}\mathcal{K}]w = \mathcal{X}\Xi. \tag{14}$$

A solution to the above equation is given by the Neumann series [8]

$$w = \mathcal{X}\Xi + \mathcal{X}\mathcal{K}\mathcal{X}\Xi + \mathcal{X}\mathcal{K}\mathcal{X}\mathcal{K}\mathcal{X}\Xi + \cdots \tag{15}$$

The first term represents the direct propagation of photons through a medium without scatter. Subsequent terms with the operator $[\mathcal{K}\mathcal{X}]^n$ represent the contribution from photons that scatter n times. The effect of the various terms in the RTE is schematically shown in Fig. [1](1).

B. Spherical Harmonics

The distribution function $w(\boldsymbol{r},\hat{s})$ is a function of five variables $\boldsymbol{r} = (x,y,z)$ and $\hat{s} = (\theta,\phi)$. If we store a sampled distribution function in a computer using 100 samples for each variable, then assuming we store the distribution function as a complex-double data structure, we could require up to 149 GB of storage. Therefore, the implementation of the RTE becomes very difficult. To solve this issue, we represent the directional portion of the distribution function in a spherical

W = XΞ + XKXΞ + XKXKXΞ + ...

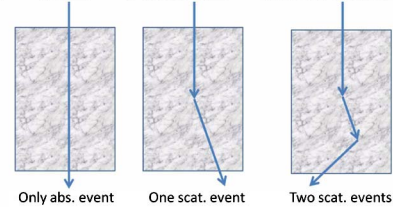Only abs. event   One scat. event   Two scat. events

Fig. 1. (Color online) A schematic illustrating the effect of the various terms of the Neumann series as light propagation occurs through the biological tissue.

harmonic basis [47]. The spherical harmonic functions are a complete and orthonormal basis for functions of $\hat{s}$. This basis is a natural way of splitting up the spatial and directional portions of a distribution function. Moreover, since the scattering kernel depends only on the angle between the direction of entrance and exit of the photons [Eq. (6)], the representation of the scattering kernel in spherical harmonics is easy and efficient.

Using spherical harmonics, we can write any distribution function as

$$w(\boldsymbol{r}, \hat{s}) = \sum_{l=0}^{\infty} \sum_{m=-l}^{l} W_{lm}(\boldsymbol{r}) Y_{lm}(\hat{s}), \qquad (16)$$

where $Y_{lm}(\hat{s})$ are the spherical harmonic functions and $W_{lm}(\boldsymbol{r})$ are the spatially dependent coefficients given by

$$W_{lm}(\boldsymbol{r}) = \int_{4\pi} \mathrm{d}\Omega Y_{lm}^*(\hat{s}) w(\boldsymbol{r}, \hat{s}). \qquad (17)$$

To illustrate the reduction in memory requirements using spherical harmonics, if we truncate the infinite series in Eq. 16 at $l = L$, then using 100 samples for x, y, and z and using $L = 4$, we require only 380 MB of storage for the entire distribution function, as opposed to the 149 GB memory that was required earlier.

For ease of notation, we represent all the spherical harmonic coefficients $W_{lm}(\boldsymbol{r})$ as a vector $\boldsymbol{W}$.

1. Scattering Operator in Spherical Harmonics
Since the scattering operator $\mathcal{K}$ depends only on the cosine of the angle between the direction of entrance and exit of the photon, it is easy to represent in the spherical harmonic basis. Let us denote the scattering operator in spherical harmonics by $\mathcal{D}$. The effect of this operator on the distribution function in spherical harmonics is given by

$$[\mathcal{D}\boldsymbol{W}]_{lm}(\boldsymbol{r}) = \sum_{l',m'} D_{lm,l'm'}(\boldsymbol{r}) W_{l'm'}(\boldsymbol{r}), \qquad (18)$$

where $D_{lm,l'm'}(\boldsymbol{r})$ denotes the kernel of the scattering operator in spherical harmonics. Using Eqs. (6) and (7), we can derive the expression for the kernel of $\mathcal{D}$ to be [8]

$$D_{lm,l'm'}(\boldsymbol{r}) = \frac{4\pi}{2l+1} k_l(\boldsymbol{r}) \delta_{ll'} \delta_{mm'}, \qquad (19)$$

where $k_l(\boldsymbol{r})$ is the scattering probability kernel represented in Legendre polynomials and δ_{ij} is the Kronecker delta function [48]. Using Eq. (6), we derive that [15]

$$k_l(\boldsymbol{r}) = \frac{c_{\mathrm{m}} \mu_s(\boldsymbol{r})}{4\pi} (2l+1) g^l. \qquad (20)$$

In a homogeneous medium, $\mu_s(\boldsymbol{r})$ is independent of position, and therefore, we can drop the dependence on $\boldsymbol{r}$ in the above equation.

2. The Attenuation Operator in Spherical Harmonics
The attenuation operator $\mathcal{X}$ is much more difficult to represent in the spherical harmonic basis. We denote the attenuation operator in spherical harmonic basis by $\mathcal{A}$. The operator $\mathcal{A}$ acting on a distribution function is given by

$$[\mathcal{A}\boldsymbol{W}]_{lm}(\boldsymbol{r}) = \sum_{l'm'} \int_{\infty} \mathrm{d}^3\boldsymbol{r}' A_{lm,l'm'}(\boldsymbol{r}, \boldsymbol{r}') W_{l'm'}(\boldsymbol{r}'), \qquad (21)$$

where, using Eq. (13), the kernel of $\mathcal{A}$ can be derived to be [8]

$$A_{lm,l'm'}(\boldsymbol{r}, \boldsymbol{r}') = \frac{1}{c_{\mathrm{m}}} \frac{1}{|\boldsymbol{r} - \boldsymbol{r}'|^2} Y_{lm}^*\left(\frac{\boldsymbol{r} - \boldsymbol{r}'}{|\boldsymbol{r} - \boldsymbol{r}'|}\right) Y_{l'm'}\left(\frac{\boldsymbol{r} - \boldsymbol{r}'}{|\boldsymbol{r} - \boldsymbol{r}'|}\right)$$
$$\times \exp\left[-\int_0^{|r-r'|} \mathrm{d}t' \mu_{\mathrm{tot}}\left(\boldsymbol{r} - t' \frac{\boldsymbol{r} - \boldsymbol{r}'}{|\boldsymbol{r} - \boldsymbol{r}'|}\right)\right]. \qquad (22)$$

This operator requires an integral over all space and a sum over all spherical harmonic coefficients to compute just one spherical harmonic coefficient in the output distribution function. Because of this reason, this operator takes the most time and memory requirements in the Neumann-series implementation, as we detail later on.

In the spherical harmonics basis, using Eq. (15), the RTE can be derived to be [8]

$$\boldsymbol{W} = \mathcal{A}\boldsymbol{\xi} + \mathcal{A}\mathcal{D}\mathcal{A}\boldsymbol{\xi} + \mathcal{A}\mathcal{D}\mathcal{A}\mathcal{D}\mathcal{A}\boldsymbol{\xi} + \cdots, \qquad (23)$$

where $\boldsymbol{\xi}$ represents the emission term [Eq. (3)] in the spherical harmonic basis.

C. Voxelization
The distribution function in spherical harmonics $W_{lm}(\boldsymbol{r})$ is still a function of the continuous vector $\boldsymbol{r}$. To discretize along the spatial coordinates, we use the voxel basis. We define the voxel basis function $\phi_i(\boldsymbol{r})$ to be 0 outside the ith voxel and 1 inside that voxel. In this basis, we represent the distribution function as

$$W_{lm}(\boldsymbol{r}) = \sum_i W_{lmi} \phi_i(\boldsymbol{r}). \qquad (24)$$

The coefficients W_{lmi} can be evaluated from $W_{lm}(\boldsymbol{r})$ as

$$W_{lmi} = \frac{1}{\Delta V} \int_{S_i} \mathrm{d}^3\boldsymbol{r} W_{lm}(\boldsymbol{r}), \qquad (25)$$

where ΔV is the volume of the voxel and S_i is the support of the voxel function $\phi_i(\boldsymbol{r})$.

The scattering operator is spatially localized and also has no spatial dependence for a homogeneous medium. Therefore, using Eqs. (19), (20), (24), and (25), we derive that the scattering operator under the voxelized representation of the distribution function is a diagonal matrix $\boldsymbol{D}$ with elements

$$D_{lm,l'm'} = c_{\mathrm{m}} \mu_s g^l \delta_{ll'} \delta_{mm'}. \qquad (26)$$

The attenuation kernel in spherical harmonics $A_{lm,l'm'}(\boldsymbol{r}, \boldsymbol{r}')$ maps from a space of functions defined in the continuous domain $\boldsymbol{r}'$ to a space of functions defined in another continuous domain $\boldsymbol{r}$. Let $u_{l'm'i'}$ denote an input distribution function represented using voxels and spherical harmonics and let v_{lmi} denote the output distribution function under the same representation after the attenuation operator has acted on $u_{l'm'i'}$. Then using Eqs. (21), (24), and (25), we derive that

$$v_{lmi} = \frac{1}{\Delta V} \sum_{l'm'i'} u_{l'm'i'} \int_{S_i} \mathrm{d}^3\boldsymbol{r} \int_{S_{i'}} \mathrm{d}^3\boldsymbol{r}' A_{lm,l'm'}(\boldsymbol{r}, \boldsymbol{r}'). \qquad (27)$$

Therefore, we deduce that the attenuation operator in the spherical harmonic and voxel basis is a matrix operator A with elements

$$A_{lmi,l'm'i'} = \frac{1}{\Delta V} \int_{S_i} \mathrm{d}^3 r \int_{S_{i'}} \mathrm{d}^3 r' A_{lm,l'm'}(\boldsymbol{r}, \boldsymbol{r}'). \qquad (28)$$

Using Eqs. (22) and (28), we derive the matrix elements for the attenuation operator.

In the spherical harmonic and voxel basis, let $\boldsymbol{\xi}_d$ and $\boldsymbol{W}_d$ be the vectors that represent the emission term [Eq. (3)] and distribution function, respectively. Then, from Eq. (23), we derive that the Neumann-series form of the RTE in the spherical harmonic and voxel basis is given by

$$\boldsymbol{W}_d = A\boldsymbol{\xi}_d + ADA\boldsymbol{\xi}_d + ADADA\boldsymbol{\xi}_d + \cdots \qquad (29)$$

In the next section, we illustrate the procedure to implement the Neumann series for a specific DOT setup using the above matrix operators.

D. Procedure

In our DOT setup, similar to the setup shown in Fig. 2, the source outputs a unidirectional beam along the optical axis, which we refer to as the z axis. The beam has uniform radiant exitance α in the x-y plane. We denote the two-dimensional (2D) profile of this beam by the function $h(x, y)$. For example, for a source emitting a uniform circular beam of diameter D, $h(x, y)$ is the cylinder function $\mathrm{cyl}(\frac{r}{D})$, where $r = \sqrt{x^2 + y^2}$ [Eq. (48)]. The beam is incident normally on a homogeneous medium with certain scattering and absorption coefficients. The emission function in the RTE is thus given by

$$\Xi(\boldsymbol{r}, \hat{s}) = \alpha\delta(z)h(x, y)\delta(\hat{s} - \hat{z}). \qquad (30)$$

The delta function on z indicates that the photons are incident only at one z-plane.

To solve the RTE in the spherical harmonic basis, we have to represent the source term in the same basis. However, to represent a collimated source in the spherical harmonic basis requires an infinite number of coefficients. To get around this difficulty, we evaluate the first term of the Neumann series numerically, and for the subsequent terms, the effect of the source is evaluated analytically. The first term $\mathcal{X}\Xi(\boldsymbol{r}, \hat{s})$ is derived by substituting the expression for the source, given by Eq. (30), in Eq. (13) and using the fact that the medium is homogeneous. This leads to

$$[\mathcal{X}\Xi](\boldsymbol{r}, \hat{s}) = \frac{\alpha}{c_{\mathrm{m}}} h(x, y)\delta(\hat{s} - \hat{z})\exp(-\mu_{\mathrm{tot}}z). \qquad (31)$$
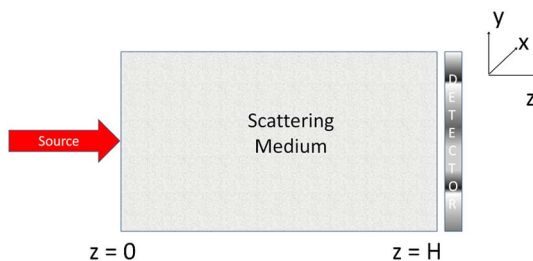

Fig. 2. (Color online) Setup for diffuse optical imaging. The defined coordinate system is shown in the top-right corner.

The flux due to this term is evaluated numerically. To account for the effect of the source term in the other terms of the Neumann series, we realize that in the Neumann series in the spherical harmonic basis [Eq. (29)], except for the first term, $\boldsymbol{\xi}_d$ is always preceded by $\boldsymbol{DA}$. In fact, it follows from Eq. (29) that an alternative way to rewrite the RTE in spherical harmonic and voxel basis is

$$\boldsymbol{W}_d = A\boldsymbol{\xi}_d + A\left[\sum_{n=0}^{\infty}(\boldsymbol{DA})^n\right](\boldsymbol{DA}\boldsymbol{\xi}_d). \qquad (32)$$

The representation of $\boldsymbol{DA}\boldsymbol{\xi}_d$ is feasible in the spherical harmonic basis since the scattering causes the collimated beam to spread out. Therefore we compute the spherical harmonic coefficients for $\boldsymbol{DA}\boldsymbol{\xi}_d$ instead. To begin with, using Eqs. (7) and (31), the term $\mathcal{KX}\Xi(\boldsymbol{r}, \hat{s})$ is derived as

$$[\mathcal{KX}\Xi](\boldsymbol{r}, \hat{s}) = K(\hat{s}, \hat{z})\frac{\alpha}{c_{\mathrm{m}}} h(x, y)\exp(-\mu_{\mathrm{tot}}z). \qquad (33)$$

Inserting the expression for $K(\hat{s}, \hat{z})$ from Eq. (6) in the above equation, we get

$$[\mathcal{KX}\Xi](\boldsymbol{r}, \hat{s}) = \frac{\mu_s \alpha}{4\pi}\left\{\frac{1 - g^2}{[1 + g^2 - 2g(\hat{s} \cdot \hat{z})]^{3/2}}\right\}h(x, y)\exp(-\mu_{\mathrm{tot}}z). \qquad (34)$$

In our coordinate system, θ is the angle that $\hat{s}$ makes with the z axis, so we replace $\hat{s} \cdot \hat{z}$ by $\cos(\theta)$. To convert the distribution function $[\mathcal{KX}\Xi](\boldsymbol{r}, \hat{s})$ to a spherical harmonic representation, we use Eq. (17). This leads to

$$[\mathcal{DA}\xi]_{lm}(\boldsymbol{r}) = \frac{\mu_s \alpha}{4\pi} h(x, y)\exp(-\mu_{\mathrm{tot}}z)$$
$$\times \int_{4\pi} \mathrm{d}\Omega \frac{1 - g^2}{[1 + g^2 - 2g\cos\theta]^{3/2}} Y_{lm}^*(\hat{s}). \qquad (35)$$

Using the generating function for Legendre polynomials, we expand the expression in g in the integrand of the above expression in terms of Legendre polynomials $P_{l'}(\cos\theta)$ as [15]

$$\frac{1 - g^2}{[1 + g^2 - 2g\cos\theta]^{3/2}} = \sum_{l'=0}^{\infty}(2l' + 1)g^{l'}P_{l'}(\cos\theta). \qquad (36)$$

Also, the spherical harmonics are given in terms of the associated Legendre polynomials as

$$Y_{lm}(\hat{s}) = (-1)^m \sqrt{\frac{2l + 1}{4\pi}\frac{(l - m)!}{(l + m)!}}P_l^m(\cos\theta)\exp(im\phi). \qquad (37)$$

Substituting the expressions from Eqs. (36) and (37) in Eq. (35), writing the integral over Ω in terms of (θ, ϕ) and rearranging the terms, we get

$$[\mathcal{DA}\xi]_{lm}(\boldsymbol{r}) = \frac{\mu_s \alpha}{4\pi} h(x, y)\exp(-\mu_{\mathrm{tot}}z)(-1)^m \sqrt{\frac{2l + 1}{4\pi}\frac{(l - m)!}{(l + m)!}}$$
$$\times \sum_{l'=0}^{\infty}(2l' + 1)g^{l'}\int_{\theta=0}^{\pi}\mathrm{d}\theta P_{l'}(\cos\theta)P_l^m(\cos\theta)\sin\theta$$
$$\times \int_{\phi=0}^{2\pi}\exp(im\phi)\mathrm{d}\phi. \qquad (38)$$

Now it can be easily shown that

$$\int_{\phi=0}^{2\pi} \exp(im\phi)\mathrm{d}\phi = \begin{cases} 2\pi, & \text{if } m = 0 \\ 0, & \text{if } m \neq 0 \end{cases}. \tag{39}$$

Therefore, $[\mathcal{DA}\xi]_{lm}(r)$ exists only for $m = 0$. To further evaluate the integral over θ for $m = 0$, we use the orthogonality relation of Legendre polynomials [48], which leads to

$$[\mathcal{DA}\xi]_{lm}(r) = \mu_s \alpha h(x,y) \exp(-\mu_{\text{tot}} z)\sqrt{\frac{2l+1}{4\pi}} \sum_{l'=0}^{\infty} g^{l'} \delta_{ll'}$$

$$= \mu_s \alpha h(x,y) \exp(-\mu_{\text{tot}} z)\sqrt{\frac{2l+1}{4\pi}} g^l. \tag{40}$$

Finally, using Eq. (25) to discretize the above equation along the spatial coordinates, we obtain the distribution function due to the $\mathcal{DA}\xi_d$ term in the different voxels to be

$$[W]_{lmi} = g^l \sqrt{\frac{2l+1}{4\pi}} \frac{\alpha\mu_s}{\Delta V \mu_{\text{tot}}} h(x_i, y_i)\{\exp[-\mu_{\text{tot}}(z_i + \Delta z)]$$

$$- \exp[-\mu_{\text{tot}} z_i]\}, \tag{41}$$

when $m = 0$. When $m \neq 0$, then the value of this term is 0. We use the distribution function due to the $\mathcal{DA}\xi_d$ term as the initial source distribution for computing the different Neumann-series terms. To evaluate these terms, in accordance with Eq. (32), we perform multiple iterations, in each of which we first apply the attenuation operation [Eq. (28)] on the source distribution, followed by the scattering operation [Eq. (19)]. At the end of each iteration, the computed distribution function is added to the Neumann series, and also used as the source for the next iteration. The iterations are applied until convergence is achieved. To evaluate whether convergence has been achieved, we use a convergence criterion that we elaborate on now.

E. Convergence Criterion

To evaluate convergence, we can consider the convergence of the distribution function at the reflected plane (the plane at which the light enters into the medium), the transmitted plane (the plane opposite to the reflected plane, also referred to as the exit face of the medium), or the total distribution function throughout the medium. We observe in simulations that the distribution function at the transmitted plane is the slowest to converge, so we evaluate the convergence of the Neumann series at this plane. To explain the criterion for convergence, we define the term η_p, which gives a measure of the photon distribution function at the transmission plane due to the pth term of the Neumann series. This term is defined as

$$\eta_p = \sum_{k,l,m} [(DA)^{p-1}\xi_d]_{lmk}, \tag{42}$$

so that the summation over k is a summation over the voxels in the transmission plane. The actual convergence criterion can be given by the contribution of the p terms of the Neumann series to the total photon distribution function. This can be measured by defining the discrete function β_p as

$$\beta_p = \frac{\sum_{j=1}^{p} \eta_j}{\sum_{j=1}^{\infty} \eta_j}. \tag{43}$$

However, while performing the Neumann-series iterations, we do not know the value of the denominator in the above expression. Therefore, we need a di–fferent convergence criterion. One might think a good idea would be to evaluate the relative contribution of the pth term of the Neumann series to the total photon distribution function that has been computed until the pth iteration. This relative contribution can be measured using the discrete function γ_p as

$$\gamma_p = \frac{\eta_p}{\sum_{j=1}^{p} \eta_j}. \tag{44}$$

We performed some experiments to validate γ_p as a convergence criterion, and found that this results in an issue, especially for a high-scattering medium. The issue is that in a high-scattering medium, while the higher-order Neumann-series terms can be quite small, leading to a small value of γ_p, the sum of these higher-order terms eventually contributes significantly to the final distribution function. Therefore, we cannot set a threshold on γ_p to define the convergence criterion, since this threshold depends on the scattering coefficient of the medium.

The difficulty with designing the convergence criteria is that after, say the Pth iteration, we do not know the values of γ_p for $p > P$, so we cannot determine the relative contribution of the terms computed after the Pth iteration to the total photon distribution function. To get around this issue, we use the empirical observation from our experiments that γ_p decreases almost linearly in logarithmic scale after a certain point and the ratio $r = \frac{\gamma_p}{\gamma_{p-1}}$ tends to a constant. As a result, the sum of the terms following γ_p is approximately $\frac{\gamma_p}{1-r}$. Thus, we define our convergence criteria using the function λ_p that is defined as

$$\lambda_p = 1 - \frac{\gamma_p}{1-r}. \tag{45}$$

This function can be used to predict convergence. As an example, we show the results obtained with an experiment, where the medium size is $4 \times 4 \times 4$ cm^3, μ_a is 0.01 cm^{-1}, and g is 0. Figure 3(a) shows the convergence of γ_p, while Fig. 3(b) shows a comparison between the actual convergence curve obtained using the variable β_p and the predicted convergence curve using λ_p. We observe that the function γ_p starts to decrease almost linearly in log scale from a certain point and its slope depends on the scattering coefficient of the medium. Also, we see that the predicted convergence given by the function λ_p matches well with the actual convergence given by the function β_p. We found this trend to be true with other experimental setups as well. Therefore, this method enables us to estimate the current convergence status and successfully stop the Neumann-series iteration when the function λ_p reaches a certain threshold. In our simulation, we set this threshold to a value of 0.9999.

Once convergence is achieved, we apply the attenuation operator for the last time. Subsequently, the distribution function at the different exit faces is determined. The procedure to obtain the flux from the distribution function is elaborated in the next section.
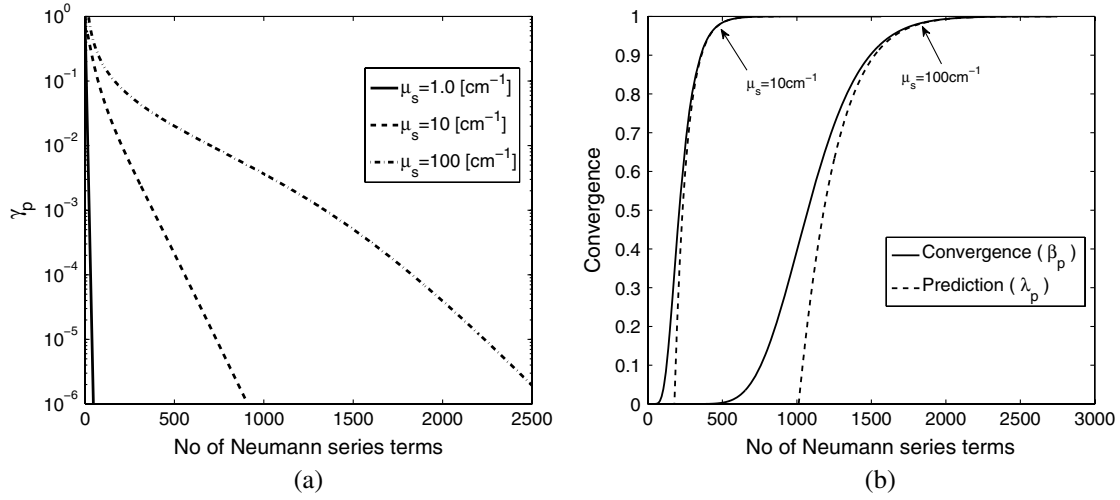
Fig. 3.   (a) The function γ_p decreases as Neumann-series iteration advances; (b) comparison between the actual convergence curve β_p and the predicted convergence curve λ_p evaluated by the distribution function at the transmitted plane.

F. Computing the Output Flux

To compute the flux at the exit or the entrance face, we must integrate the distribution function over space and angles. In this subsection, we describe the procedure to compute the transmitted flux. The theory for computing the reflected flux is similar. The radiant energy measured by the ith pixel of the detector is given by

$$Q_i = \int_P d^2 r \int_{2\pi} d\Omega \int_0^\tau dt d_i(\mathbf{r}, \hat{s}, t) w(\mathbf{r}, \hat{s}, t)(\hat{\mathbf{n}} \cdot \hat{s}), \qquad (46)$$

where d_i denotes the detector sensitivity for the ith pixel and $\hat{\mathbf{n}}$ is the normal outward vector at the detector plane. In this study, we consider a contact detector with the detector plane parallel to the transmitted face of the medium, or alternatively normal to the source, so that $\hat{\mathbf{n}} = \hat{z}$. The detector is also assumed to have uniform sensitivity over the whole pixel and has the same x-y pixelization as the distribution function. We consider a time interval of 1 s, since we are interested in determining the flux in units of watts. For this case, the transmitted flux is given by

$$\Phi_i = c_{\mathrm{m}} \Delta x \Delta y \int_{2\pi} d\Omega(\hat{z} \cdot \hat{s}) w(x_i, y_i, H, \hat{s}), \qquad (47)$$

where (x_i, y_i) denote the x and y coordinates of the center of the ith detector pixel and $z = H$ corresponds to the detector plane. In this expression, the integral is over the 2π steradians since we only consider photons that are traveling in the direction of the detector. The speed of light in the medium appears in this equation to determine the number of photons crossing the detector plane in a 1 s interval. Writing the distribution function $w(x_i, y_i, H, \hat{s})$ in spherical harmonics,

$$\Phi_i = c_{\mathrm{m}} \Delta x \Delta y \int_0^{\pi/2} d\theta \, \sin \theta \, \cos \theta \int_0^{2\pi} d\phi \sum_{lm} W_{lmi'} Y_{lm}(\theta, \phi), \qquad (48)$$

where i' refers to the voxel that is in contact with the ith pixel on the detector. Using Eqs. (37) and (39), the integral over ϕ is nonzero only for $m = 0$, for which case, it is equal to 2π. Thus, the above equation simplifies to

$$\Phi_i = 2\pi c_{\mathrm{m}} \Delta x \Delta y \sum_l W_{l0i'} \sqrt{\frac{2l+1}{4\pi}} \int_0^{\pi/2} d\theta \, \sin \theta \, \cos \theta P_l(\cos \theta), \qquad (49)$$

where we have also replaced the spherical harmonic function $Y_{lm}(\theta, \phi)$ with its form in Legendre polynomials. Making a change of variables, we arrive at the final expression for the transmitted flux as

$$\Phi_i = 2\pi c_{\mathrm{m}} \Delta x \Delta y \sum_l W_{l0i'} \sqrt{\frac{2l+1}{4\pi}} \int_0^1 du P_l(u) u. \qquad (50)$$

There are closed-form solutions for the integral in Eq. (50). Using these equations, we determine the transmitted flux. The reflected flux can also be computed similarly.

In this section, we have established the theoretical foundations to simulate light propagation in optical imaging using the Neumann-series version of the RTE. We now discuss the implementation of the algorithm.

3. IMPLEMENTATION

The software to implement the Neumann-series algorithm is developed in the C programming language on a 2.26 GHz Intel Quad core system running 64 bit Linux. The flowchart of our implementation is shown in Fig. 4. In the software, after reading the input-phantom specifications, the $\mathbf{DA}\boldsymbol{\xi}_d$ term is computed using Eq. (41). Subsequently, in each iteration of the Neumann series, the attenuation operator is applied, followed by the scattering operator. While the scattering operator is easy to apply since it is a diagonal operator, the attenuation operator is considerably difficult to apply. This is due to two reasons: first that the attenuation operator itself is computationally very intensive, and second that its implementation requires the distribution function values of all the voxels that surround it.

There are two methods to implement the attenuation operation. The first method is to apply the attenuation operator in every iteration of the Neumann series. However, such an implementation requires considerable execution time, to the order of days, even for simple phantoms, since for every voxel,

Read input
phantom
configuration

Compute distribution
function to DAξ$_d$ term

Generate the terms of
the A matrix

Apply attenuation
operator

Apply scattering
operator

Convergence
achieved ?   → No

↓ Yes

Apply attenuation
operator

Compute total
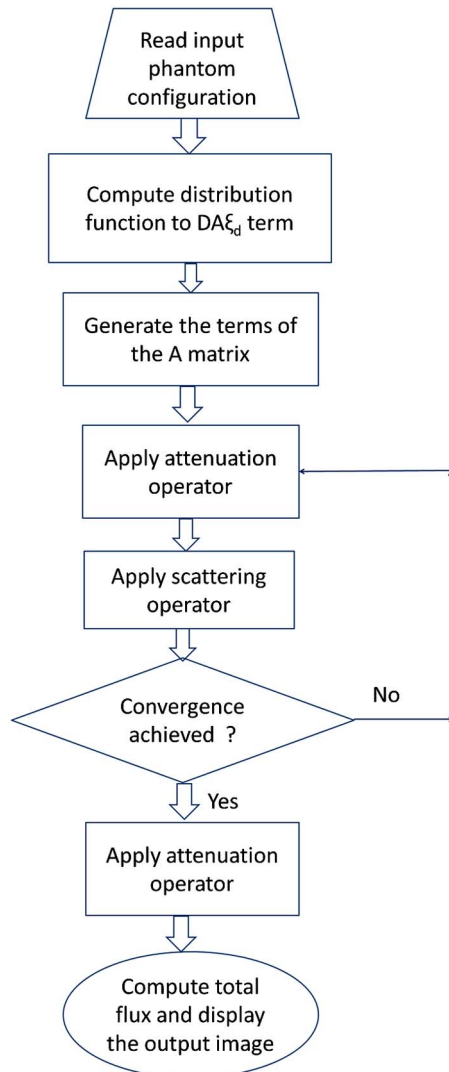flux and display
the output image

Fig. 4.   (Color online) Flowchart of our implementation for the Neumann-series form of the RTE.

we have to carry out the computationally intensive operation of accounting for the effect due to all the other voxels. If there are N voxels, the amount of time required is proportional to N^2. The second approach is to precompute and store the terms $A_{lm,l'm'}(i, i')$, for each pair of voxels i and i', since the same terms are required in each Neumann-series iteration. However, this requires a considerable amount of memory even for small phantoms. The attenuation kernel is stored as a complex-double data structure, which implies that every element of this kernel typically requires 32 bytes of memory. Consider the value of l varying from 0 to L, so that, for each voxel, the number of spherical harmonic coefficients required is $(L + 1)^2$. If there are N voxels, then the amount of memory required to store the elements of the attenuation kernel is $32 \times N^2 (L + 1)^2$ bytes of memory. Even for a $20 \times 20 \times 20$ phantom, considering the value of L to be 1, this translates to about 8 GB of memory requirement. Furthermore, the memory requirements scale as the square of the number of voxels. These factors increase the memory requirements of the software significantly.

However, a very useful simplification of the attenuation kernel occurs in uniform media. Since the attenuation coefficient

is a constant in uniform media, in Eq. (22), the exponential factor becomes equal to $\exp(-\mu_{tot}|\boldsymbol{r} - \boldsymbol{r}'|)$, so that the terms of the attenuation kernel simplify to

$$A_{lm,l'm'}(\boldsymbol{r}, \boldsymbol{r}') = \frac{1}{c_m} \frac{1}{|\boldsymbol{r} - \boldsymbol{r}'|^2} Y_{lm}^* \left(\frac{\boldsymbol{r} - \boldsymbol{r}'}{|\boldsymbol{r} - \boldsymbol{r}'|} \right) Y_{l'm'} \left(\frac{\boldsymbol{r} - \boldsymbol{r}'}{|\boldsymbol{r} - \boldsymbol{r}'|} \right)$$
$$\times \exp(-\mu_{tot}|\boldsymbol{r} - \boldsymbol{r}'|). \tag{51}$$

Thus the elements $A_{lm,l'm'}(\boldsymbol{r}, \boldsymbol{r}')$ are functions of only $\boldsymbol{r} - \boldsymbol{r}'$, or alternatively the operator $\mathcal{A}$ is shift-invariant for a uniform medium. Because of this simplification, we need to store the attenuation kernel elements only as a function of the vectors that join two voxels. Consequently, the memory requirements scale linearly as the number of voxels and not exponentially. As an illustration of the reduction in memory requirements, in the example that we cited above with $N = 20^3$ and $L = 1$, the memory required to store the terms of the A matrix reduces from 8 GB to 2 MB, and thus this matrix can be easily stored in the main memory of the computing system.

In our implementation of the Neumann-series RTE for uniform media, we use the above simplification and precompute and store the terms of the attenuation kernel as a function of the vector joining these voxels. After this, in accordance with Eq. (32), in every iteration of the Neumann series, the attenuation operator is applied [Eq. (28)], followed by the scattering operator [Eq. (26)]. The resulting term is added to the total distribution function, and also used as the source for the next iteration. This process is repeated until convergence is achieved, based on the criterion defined in Eq. (45). Once convergence is achieved, the attenuation operator is applied again. The flux due to the computed terms, obtained using Eq. (50), is added to the flux due to the $\mathcal{X}\Xi$ term, and finally, the output image is displayed.

Another simplification arises when we simulate the RTE for an isotropic medium, i.e., the medium for which $g = 0$. From Eq. (19), for $g = 0$, the elements of the scattering operator D become 0 whenever $l > 0$. Therefore, the scattering operation zeros out all the spherical harmonic coefficients of the distribution function with $l > 0$. Consequently, in all the attenuation operations that are followed by a scattering operation, we do not evaluate the distribution function for $l > 0$. This also reduces the computational requirements significantly, since we do not evaluate a number of distribution function coefficients.

4. EXPERIMENTS AND RESULTS

We assess the performance of the Neumann-series RTE approach by comparing the output obtained using the Neumann-series algorithm with the output obtained using Monte Carlo (MC) simulations. MC results are considered as the gold standard output to study the propagation of photons in a scattering medium in biomedical optics. We obtained the MC results using a software that we developed based on the MC multilayered (MCML) tissue package [49]. In our MC experiments, the number of photons was 10^8.

A. Experiment 1: Scattering Medium with $\mu_s H = 1$
The objective of this experiment is to evaluate the accuracy of the Neumann-series form of the RTE. The simulation setup is similar to the experimental setup in Chai *et al.* [50]. The scattering medium is a cube, as illustrated in Fig. 5. The entire top surface is subjected to a normal collimated incident beam, and
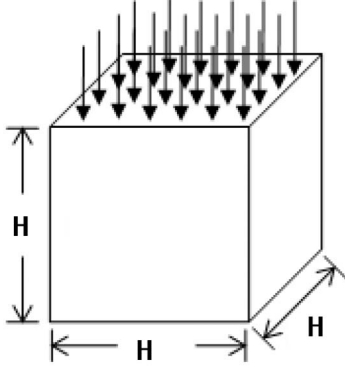
Fig. 5.   Illustration of the setup for Experiment 1.

the other walls are nonreflective boundaries. The medium is nonabsorptive and isotropic and has a scattering coefficient μ_s and length H such that $\mu_s H = 1$.

From our initial experiments, we found that the accuracy of the RTE implementation is dependent on the length of the voxel, also referred to as the grid size, and its relation to the mean free path (mfp). The mfp is the mean distance that a photon travels before being scattered, and is equal to the

inverse of the scattering coefficient of the medium. To study this dependence further, in the Neumann-series simulation, we change the spatial grid size Δx from 0.04 to 0.2 mfp. For this experiment, we measure a normalized dimensionless flux q_i for each pixel, which is defined as

$$q_i = \frac{\Phi_i}{\alpha \Delta x \Delta y}, \tag{52}$$

where α is the radiant exitance of the beam as defined earlier, and the flux Φ_i is computed using Eq. (50). In Figs. 6(a)–6(d), we present the linear intensity profile from the line passing through the center of the output image, determined using RTE and MC for this experimental setup for different values of grid sizes Δx. The value of L, the maximum value of l in the spherical harmonic expansion, is kept as 3. As we observe, there is a very good agreement between the MC and RTE outputs for transmitted, reflected and side-wall fluxes, especially when the grid size Δx is small. A slight discrepancy is visible in the reflected flux when the grid size is larger than 0.1 mfp. The transmitted and side-wall fluxes show very good match with MC results even when the grid size is 0.2 mfp.
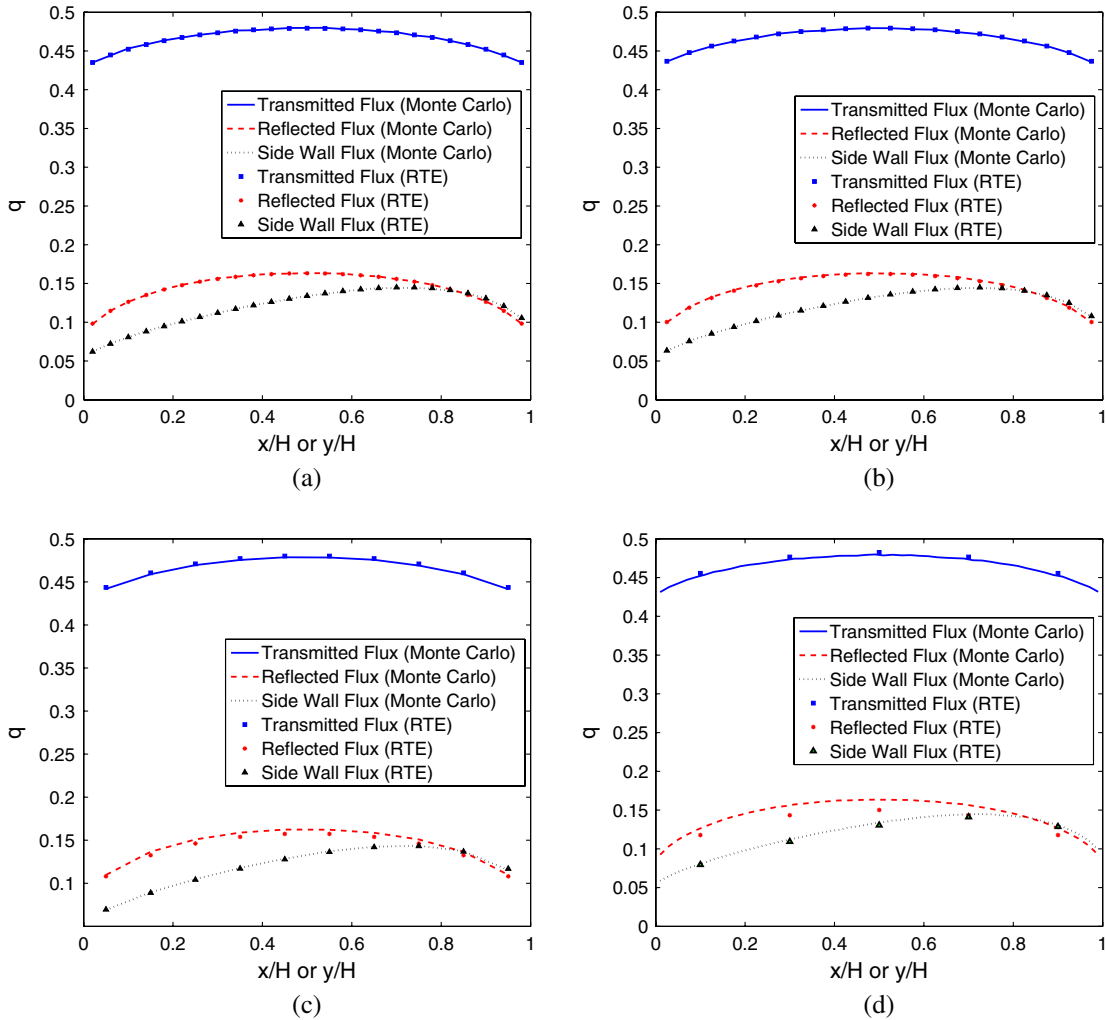

Fig. 6.   (Color online) Comparison results between the RTE solver and MC simulation with different spatial grid size Δx: (a) $\Delta x = 0.04$ mfp; (b) $\Delta x = 0.05$ mfp; (c) $\Delta x = 0.1$ mfp; (d) $\Delta x = 0.2$ mfp.
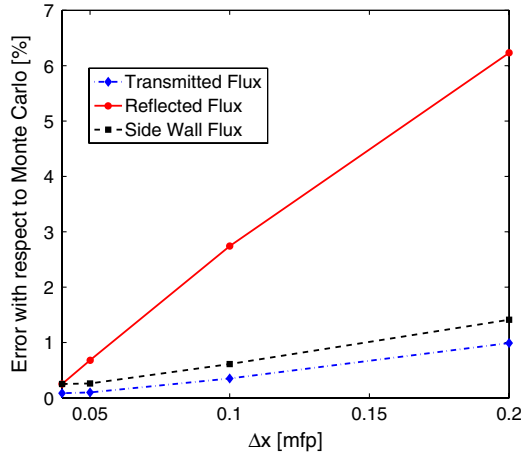
Fig. 7.   (Color online) Average percent error of the RTE solver with respect to MC as a function of grid size Δx.

To quantify the accuracy of the RTE, we define the percent error $\epsilon_{\mathrm{RTE,MC}}$ between the RTE and the MC results as

$$\epsilon_{\mathrm{RTE,MC}} = \sum_i \frac{|\Phi_{i,\mathrm{RTE}} - \Phi_{i,\mathrm{MC}}|}{\Phi_{i,\mathrm{MC}}} \times 100, \qquad (53)$$

where $\Phi_{i,\mathrm{RTE}}$ and $\Phi_{i,\mathrm{MC}}$ denote the computed flux for the ith pixel using the RTE and MC simulations, respectively, and the summation is over the pixels of the detector. Figure 7 shows the error as a function of spatial grid size Δx, where Δx is expressed in terms of mfp. We also present the error for the flux transmitted through the side-walls of the medium. The error is less than 1% for the transmitted, reflected, and side-wall fluxes, if the condition $\Delta x = 0.05$ mfp is satisfied. The error increases with the grid size significantly in reflected flux. However, the increase in error of transmitted and side-wall fluxes is minor and the error is still around 1.0% even when the grid size is 0.2 mfp.

B. Experiment 2: Ability to Handle Collimated Source

To further confirm the accuracy of the RTE for medium with higher values of $\mu_s H$, and to study its advantages compared

to using the diffusion approximation, we perform another experiment. In this experiment, the scattering medium is an isotropic medium, shaped as a cube, with a length of 5 mfp. The medium is irradiated by a collimated pencil beam incident on the medium, illuminating only the center of its top surface. The spatial grid size Δx is kept as 0.1 mfp and the number of spherical harmonic coefficients is kept as $L = 1$ and $L = 3$ for the two experiments, respectively. In addition to the MC simulation, the output fluxes are also obtained using the diffusion equation (DE). To compute the result using the DE, commercial finite element software called COMSOL Multiphysics TM (www.comsol.com) is used. With the diffusion approximation, it is very complicated to model a collimated source, especially for the thin media in our experiment [51–53]. Therefore, for the DE-based method, we model our source as a diffuse boundary source with a Robin boundary condition that no reflection occurs at the surface [11,51].

The results for the transmitted and reflected fluxes are shown in Fig. 8. We observe from the figure that the RTE $(L = 3)$ and MC results are almost identical but the DE result deviates from the MC result. Moreover, the DE result does not exhibit the peak in the transmitted profile that appears in both the RTE and MC results. While the RTE solution with $L = 1$ is not very accurate, it is still better than the DE solution.

This result highlights some important points of the Neumann-series implementation. The first point this result illustrates is the ability of the RTE to handle collimated sources. A well-known issue with the standard-diffusion-approximation-based methods is their inability to model collimated light sources accurately [52,53]. As the results of this experiment show, the Neumann-series implementation can easily handle collimated sources and produce more accurate output than the DE, even with the simple $L = 1$ approximation. The second point this result highlights is the accuracy that the Neumann-series implementation achieves due to the way it handles the different components of light. The scattered component is treated differently from the nonscattered component. The latter is evaluated numerically in the normal $(\mathbf{r}, \hat{s})$ basis, and subsequently added to the output. Therefore,
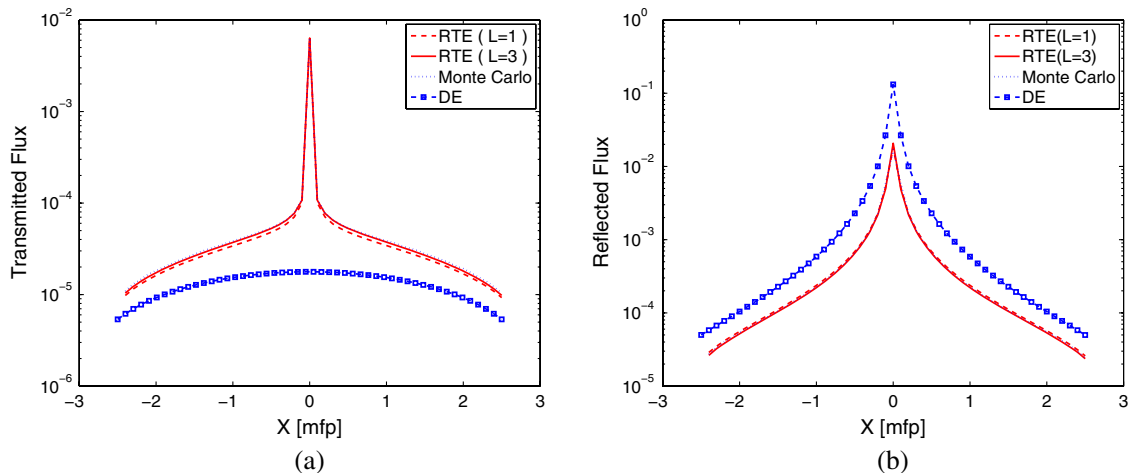

Fig. 8.   (Color online) Comparison between the results from the RTE, MC, and DE in (a) transmitted flux and (b) reflected flux. The optical parameters are $\mu_a = 0.1$ cm^{-1}, $\mu_s H = 5.0$, $g = 0$. The voxel size Δx is 0.1 mfp. The fluxes are plotted in arbitrary units (a.u.).
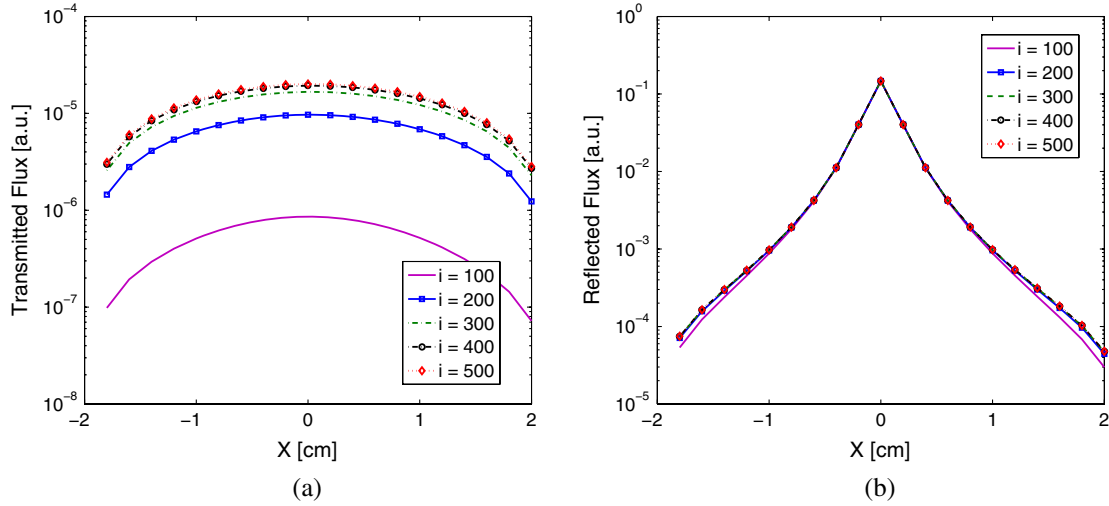
Fig. 9. (Color online) Computed (a) transmitted flux and (b) reflected flux shown as a function of the number of Neumann-series terms. We observe that these flux values converge as the number of Neumann-series terms increases.

the nonscattered component is computed very accurately. This accuracy is not possible if we evaluate the nonscattered component of light in a spherical harmonics basis. Finally, this result also shows that using the RTE, we can model light propagation in a relatively thicker medium where $\mu_s H = 5$.

C. Experiment 3: Convergence with Increasing Number of Neumann-Series Terms

We find in all our experiments that the RTE solution converges with an increase in the number of terms in the Neumann series. As an illustrative example, we consider an experimental setup as in Fig. 5 with a cube-shaped medium of dimensions $4 \times 4 \times 4$ cm^3 that has optical properties as $\mu_s = 10$ cm^{-1}, $\mu_a = 0.01$ cm^{-1}, and $g = 0$. The number of terms in the Neumann series is increased and the transmitted and reflected fluxes are determined. The linear profiles of these fluxes are shown in Fig. 9. We observe that both the transmitted and reflected fluxes converge with an increase in the number of Neumann-series terms, and the speed of convergence is much slower for the transmitted flux as compared to the reflected flux.

D. Experiment 4: Convergence with Increasing Number of Spherical Harmonics

The objective of this set of experiments is to confirm the convergence of the Neumann-series method as the number of spherical harmonics is increased. We also compare the results of the RTE with MC results to confirm whether the convergence is towards the correct solution. While convergence towards the MC results would help validate the Neumann-series form of the RTE, the results would also provide insights on the number of spherical harmonic coefficients required to achieve convergence for different kinds of scattering media.

The requirement for many spherical harmonics to represent the distribution function emerges when the scattering is anisotropic, since in that case, the photon propagation is more directional. Therefore, for this study, we experiment with two different types of media: the first is an isotropic-scattering medium $(g = 0)$, and the second is an anisotropic-scattering medium with $g = 0.8$. The medium has a cubic shape, nonreflective boundaries, and an optical length $\mu_s H$ of unity. A collimated pencil beam is incident on a cubic-shaped scattering medium, illuminating only the center of the top surface. The
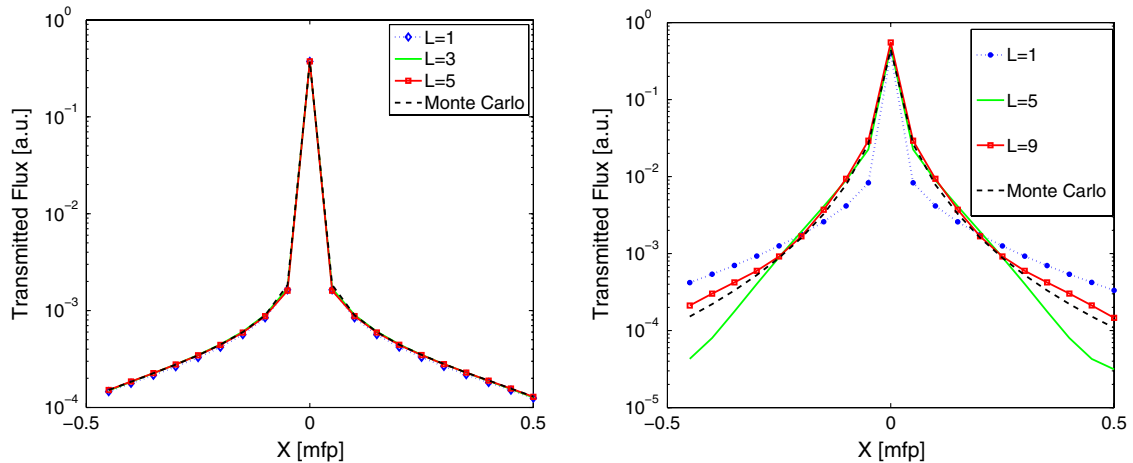

Fig. 10. (Color online) Convergence of the Neumann-series RTE with spherical harmonics: (a) transmitted flux with $g = 0$ and (b) transmitted flux with $g = 0.8$. In each figure, the MC result is also plotted.
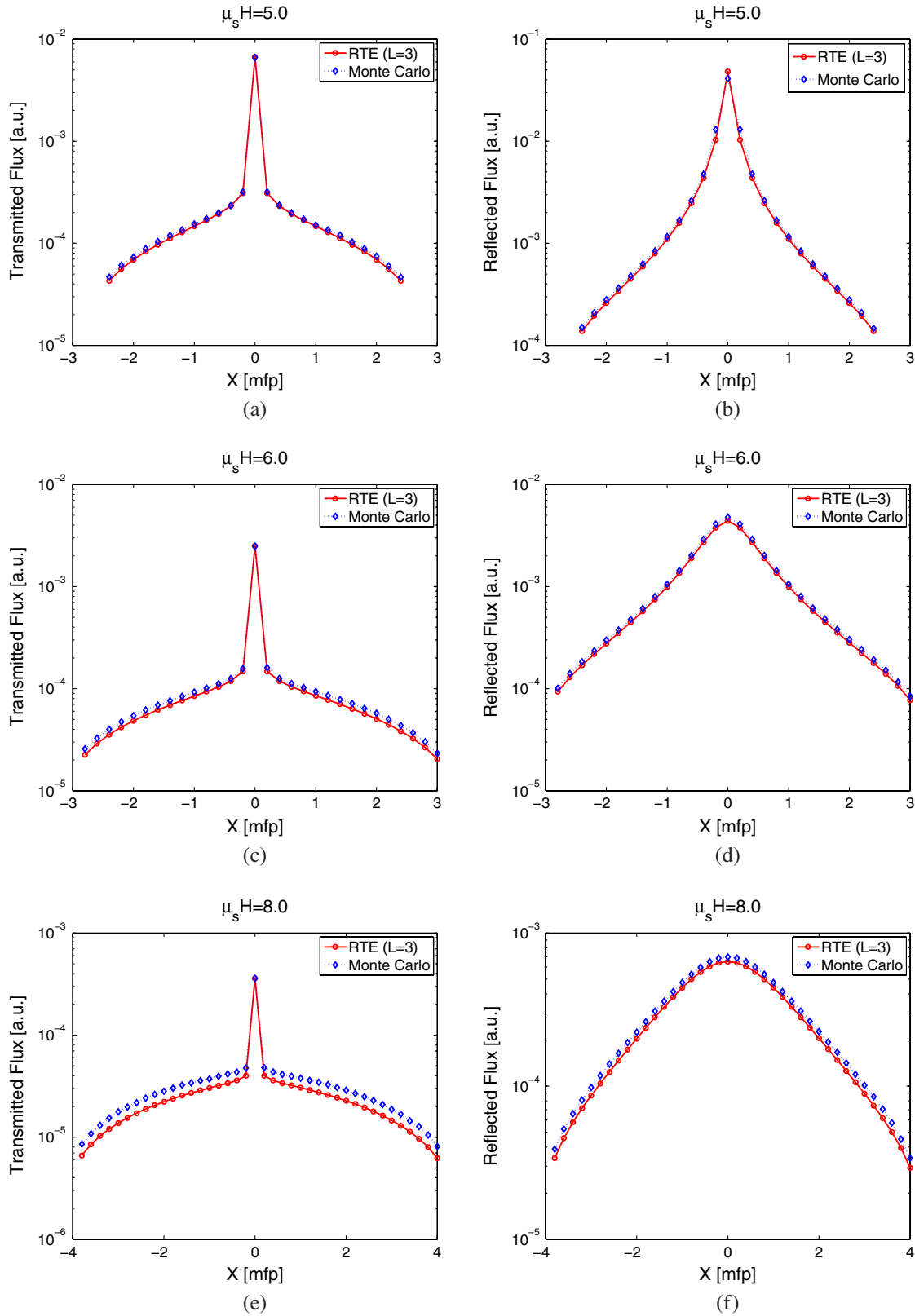
Fig. 11.   (Color online) Comparison of the Neumann-series RTE ($L = 3$) and MC results for the transmitted and reflected fluxes, respectively, with different values of $\mu_s H$. The different cases are (a), (b) $\mu_s H = 5$; (c), (d) $\mu_s H = 6$; (e), (f) $\mu_s H = 8$; (g), (h) $\mu_s H = 9$; (i), (j) $\mu_s H = 10$. The value of Δx is 0.2 mfp for these experiments, and the optical parameters of the medium are $\mu_a = 0.1$ cm^{-1} and $g = 0$. *Continues on next page.*

results are shown in Fig. 10. In the isotropic-scattering medium, the linear profile of the transmitted flux obtained with $L = 1$ matches well with MC results as shown in Fig. 10(a).

Increasing the value of L to 3, and then to 5, does not cause any change in the result, indicating convergence of the RTE.

$\mu_s H = 9.0$ (g)

$\mu_s H = 9.0$ (h)

$\mu_s H = 10.0$ (i)

$\mu_s H = 10.0$ (j)
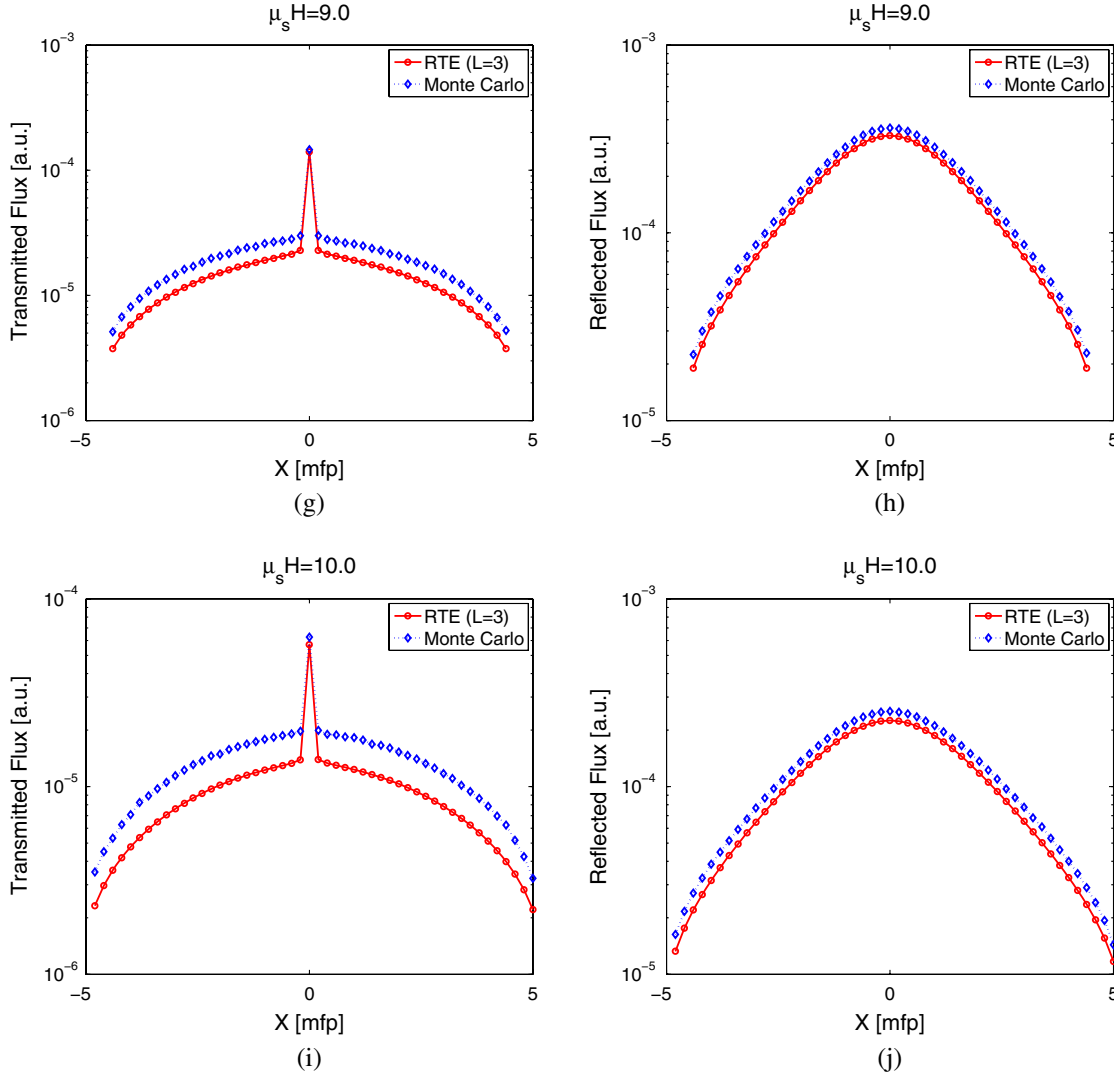
Fig. 11.   (Color online) *Continued.*

The results for the anisotropic-scattering medium are shown in Fig. 10(b). We observe that the $L = 1$ approximation is not accurate for this scenario. This is expected since as the value of g increases, the scattering becomes more forward-biased. Consequently, many spherical harmonic coefficients are required to represent the distribution function. We observe that as the value of L increases, the solution of the RTE implementation converges toward the MC result. When $L = 9$, we see a very good match between the MC and the RTE result. Thus, although the RTE result does eventually converge to the MC result for media with high values of g, this requires a large number of spherical harmonic coefficients. This in turn requires significant memory and computational resources.

E. Experiment 5: Performance of RTE with Increasing Value of $\mu_s H$

We perform this set of experiments to test the performance of the RTE as the number of scattering events in the medium, or alternatively the value of $\mu_s H$ of the medium is increased. We have seen earlier in Subsection 4.B that with a $\mu_s H$ of 5, the RTE can model photon propagation accurately. Therefore, in this experiment, we increase the length of the medium such
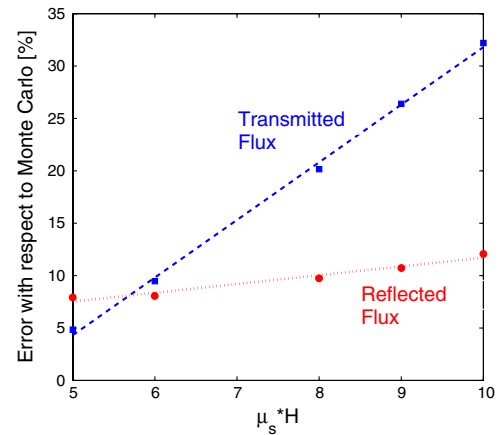

Fig. 12.   (Color online) Error between the RTE and MC results as a function of the optical length of the medium. The $L = 3$ approximation and $\Delta x = 0.2$ mfp are used in the simulation. The dotted lines are superimposed on the errors to demonstrate the observation that the error varies approximately linearly with the optical length.

Table 1. Computation Time Required by the RTE Implementation for the Various Simulations Performed in this Paper[a]

Test case	No. of voxels $(nX \times nY \times nZ)$	L	$n$terms	$\mu_s H$	MFP	g	Time in s
Fig. 6(a)	$25 \times 25 \times 25$	3	10	1	0.04	0	414
Fig. 6(b)	$20 \times 20 \times 20$	3	10	1	0.05	0	136
Fig. 6(c)	$10 \times 10 \times 10$	3	10	1	0.10	0	27
Fig. 6(d)	$5 \times 5 \times 5$	3	10	1	0.20	0	9
Fig. 8	$50 \times 50 \times 50$	3	46	5	0.10	0	70584
Fig. 10(a)	$20 \times 20 \times 20$	1	11	1	0.05	0	24
Fig. 10(a)	$20 \times 20 \times 20$	3	11	1	0.05	0	131
Fig. 10(b)	$20 \times 20 \times 10$	1	13	1	0.05	0.8	15
Fig. 10(b)	$20 \times 20 \times 10$	3	9	1	0.05	0.8	117
Fig. 10(b)	$20 \times 20 \times 10$	5	9	1	0.05	0.8	651
Fig. 10(b)	$20 \times 20 \times 10$	7	9	1	0.05	0.8	2440
Fig. 10(b)	$20 \times 20 \times 10$	9	9	1	0.05	0.8	9423
Fig. 11(a)	$25 \times 25 \times 25$	3	46	5	0.20	0	467
Fig. 11(c)	$30 \times 30 \times 30$	3	58	6	0.20	0	1308
Fig. 11(e)	$40 \times 40 \times 40$	3	86	8	0.20	0	12749
Fig. 11(g)	$45 \times 45 \times 45$	3	101	9	0.20	0	30948
Fig. 11(i)	$50 \times 50 \times 50$	3	116	10	0.20	0	72118

[a]In the table headings, nX, nY, and nZ correspond to the number of voxels along the x, y, and z axes, respectively, L corresponds to the maximum value of l in the spherical harmonic expansion, $n$terms is the number of Neumann-series terms, MFP refers to the mfp, g is the anisotropy factor, and the computation time is measured in seconds.

that the value of $\mu_s H$ changes from 5 to 10. The voxel size is kept as $\Delta x = 0.2$ mfp. The experimental setup consists of a laser source with a circular beam profile illuminating only the center of the top surface of the medium. The diameter of the incident beam is the same as the voxel size, and, therefore, varies depending on the scattering coefficient of the medium. The absorption coefficient of the medium is $\mu_a = 0.1$ cm^{-1}. As in the previous test cases, the boundaries of the medium are nonreflective.

The result from the RTE implementation and MC are shown in Fig. 11. It is seen that the RTE result deviates from the MC result as the value of $\mu_s H$ increases. This deviation is quite significant for the transmitted flux. We believe that this deviation is due to the small errors in the computation of the Neumann-series terms arising as a result of insufficient discretization of the medium. The errors continuously

propagate in the computation of the higher-order Neumann-series terms, due to the way the algorithm is implemented. These errors are not apparent when the value of $\mu_s H$ is small, since then, the number of Neumann-series terms required to compute the distribution function is also small. However, the errors start appearing when the number of Neumann-series terms is high. This happens in a medium with a high value of $\mu_s H$, since in such a medium, the number of scattering events is large. The spatial discretization of $\Delta x = 0.2$ mfp may be insufficient in a medium with large value of $\mu_s H$, and we believe that this issue will not appear if the grid size is made sufficiently small. Because of memory limitations, we cannot decrease the spatial grid size any further, so we cannot confirm this hypothesis currently. However, with the increase in memory capacity of computational systems, such a confirmation will be possible in the near future.

We also quantitatively measure the error in the RTE result with respect to the MC result using Eq. (53). As shown in Fig. 12, the error increases linearly with the value of $\mu_s H$. Since the number of terms in the Neumann series increases approximately linearly with the value of $\mu_s H$, this supports our earlier hypothesis regarding the error being due to propagation of the inaccuracies in the computation of the Neumann-series terms. The rise in error in reflected flux is quite slow compared to transmitted flux, and the error in transmitted flux surpasses the error in reflected flux at $\mu_s H = 6.0$. A possible reason for this can be that the reflected flux converges faster, i.e., within a smaller number of Neumann-series terms, in contrast to the transmitted flux. Therefore, the computational error does not propagate significantly while computing the reflected flux.

F. Computational Requirements
In this subsection, we discuss the performance of the Neumann-series RTE in terms of the computational-time requirements for the simulation studies that we have performed above. These simulation studies were done on a Linux server with 20 Intel Xeon 2.4 GHz processors and 256 GB RAM. The 20 available processors were used through the open multiprocessing (OpenMP) application programming interface. In addition, except for the Neumann-series iterations, the rest of the computations were performed on just the main
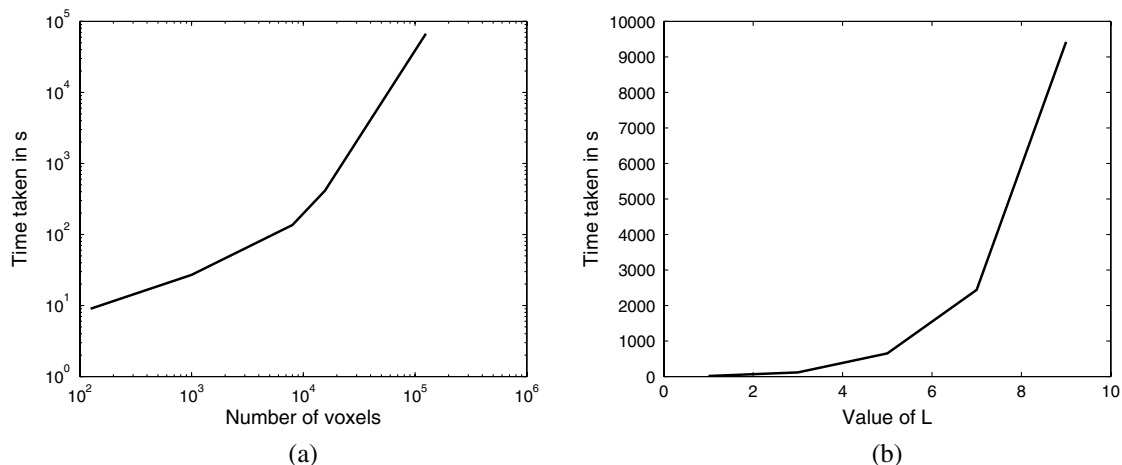

(a)

(b)

Fig. 13.   (a) Plot of computation time versus number of voxels based on Fig. 6 simulations. (b) Plot of computation time versus number of spherical harmonics based on Fig. 10 simulations.

processor. Table 1 summarizes the computation time of our implementation for the different experiments that we performed.

We plot the computation time as the number of voxels is increased for the test cases in the experiment corresponding to Figs. 6(a)–6(e). The plot is on a logarithmic scale and is shown in Fig. 13(a). We observe that the computation time increases rather linearly with the number of voxels in the medium. In fact, the slope of the logarithmic curve is less than unity. However, the plot also shows that the computational-time requirements become significantly high when the number of voxels is high. As we have seen in the previous experiments, to achieve accurate RTE output, it is necessary to have small voxel sizes. An increase in the phantom size corresponds to a substantial increase in the number of voxels. With the requirement of a higher number of voxels, achieving good computational efficiency becomes difficult.

We also plot the computation time as the number of spherical harmonic coefficients is increased, for the test cases in the experiment corresponding to Fig. 10. In this set of experiments, the value of L for the spherical harmonic basis is increased from 1 to 9, which in turn corresponds to the total number of spherical harmonic coefficients increasing from 4 to 100. The plot is shown in Fig. 13(b). We observe that as the number of spherical harmonic coefficients increases, the computational time of the code increases quite significantly. For an anisotropic-scattering medium, as we have seen from the experiments in Subsection 4.D, the number of spherical harmonic coefficients required is quite large. Thus, in such a medium, achieving good computational efficiency is time consuming.

5. DISCUSSION AND CONCLUSIONS

In this paper, we suggest an implementation of the Neumann-series form of the RTE for optical imaging. The mathematical methods are developed and the software is designed to implement the RTE for a diffuse-optical-imaging setup. We then perform an exhaustive analysis of the accuracy, speed, and convergence characteristics of the RTE implementation for this setup. We evaluate the accuracy of the implementation by comparing its results to MC outputs for different kinds of media. We also verify the convergence of the RTE as the number of Neumann-series terms, and the number of spherical harmonic coefficients is increased. Finally, we also present an analysis of the computational requirements of the RTE. We observe that as the number of voxels or spherical harmonics increases, the computational time required by the RTE increases to very high values.

From our results, we also show that the Neumann-series form of the RTE can model collimated laser sources, which is very complicated to perform using methods based on the standard diffusion approximation. This is very important since in various DOT setups, the source is either a single or a combination of laser-beam-like collimated sources. Also, the RTE can easily simulate light propagation in a medium with small values of $\mu_s H$, where the diffusion approximation fails. Another issue with the diffusion approximation is that it breaks down when the absorption coefficient is close to the scattering coefficient. We found from experiments that the RTE can also model photon propagation accurately in this scenario, with very good computational efficiency [54]. Therefore,

the Neumann-series RTE can handle many such situations easily where the diffusion-approximation-based methods do not work.

The simulated results also show that the Neumann-series implementation generates accurate results until the spatial grid size is small. A medium that has a high value of $\mu_s H$ requires many voxels. For example, for $\mu_s H$ equal to 10, the number of voxels required along each dimension in a cube-shaped medium is about 100. Therefore, the discretization requires 100^3 voxels, which increases the computational time significantly, and also requires large memory. Since the computational time and the memory requirement of the RTE increases to high values as the number of voxels is increased, this places a limitation on the Neumann-series approach. However, for this high a value of $\mu_s H$, the diffusion approximation gives accurate results. The advantage of the Neumann-series method is that it works in many cases where the methods using diffusion approximation fail. Therefore, based on our study, it will perhaps be useful to develop a scheme that uses the methods based on diffusion approximation or the Neumann-series method, based on the type of medium being investigated. Another advantage of the Neumann-series method, as opposed to the differential methods to solve the RTE, is that instead of requiring the solution of a number of coupled differential equations, the Neumann-series method just requires the solution of one equation. This framework might prove to be useful in some applications. Also, with an increase in computational capability, the time required by the integral version of the RTE will continue to decrease.

In general, however, we can infer from our research that the Neumann-series RTE algorithm is computationally quite intensive. For a nonuniform medium, the computational requirements increase even further, since for a nonuniform medium, the attenuation operator is no longer shift-invariant. In many cases, the various media through which we are interested in simulating light propagation in optical imaging are heterogeneous. Therefore, we have, in parallel, been working on developing the Neumann-series form of the RTE for nonuniform media. The initial implementation that we programmed on sequential processing architectures takes considerable execution time. Therefore, we have worked on developing this algorithm on the NVIDIA graphics processing units (GPUs). This implementation has helped us gain significant speedups. We have submitted another paper based on this work [54].

REFERENCES

1. A. P. Gibson, J. C. Hebden, and S. R. Arridge, "Recent advances in diffuse optical imaging," Phys. Med. Biol. **50**, R1–R43 (2005).
2. D. A. Boas, D. H. Brooks, E. L. Miller, C. A. DiMarzio, M. Kilmer, R. J. Gaudette, and Q. Zhang, "Imaging the body with diffuse optical tomography," IEEE Signal Process. Mag. **18**, 57–75 (2001).
3. A. Gibson and H. Dehghani, "Diffuse optical imaging," Phil. Trans. R. Soc. A **367**, 3055–3072 (2009).
4. A. A. Tanbakuchi, A. R. Rouse, and A. F. Gmitro, "Monte Carlo characterization of parallelized fluorescence confocal systems imaging in turbid media," J. Biomed. Opt. **14**, 044024 (2009).
5. J. Chen, V. Venugopal, and X. Ante's, "Monte Carlo based method for fluorescence tomographic imaging with lifetime multiplexing using time gates," Biomed. Opt. Express **2**, 871–886 (2011).
6. M. Y. Kirillin, I. V. Meglinskii, and A. V. Priezzhev, "Effect of photons of different scattering orders on the formation of a signal in optical low-coherence tomography of highly scattering media," Quantum Electron. **36**, 247–252 (2006).
7. K. Takagi, H. Haneishi, N. Tsumura, and Y. Miyake, "Alternative oblique-incidence reflectometry for measuring tissue optical properties," Opt. Rev. **7**, 164–169 (2000).
8. H. H. Barrett and K. J. Myers, *Foundations of Image Science*, 1st ed. (Wiley, 2004).
9. S. R. Arridge, M. Schweiger, M. Hiraoka, and D. T. Delpy, "A finite element approach for modeling photon transport in tissue," Med. Phys. **20**, 299–309 (1993).
10. H. Dehghani, B. Brooksby, K. Vishwanath, B. W. Pogue, and K. D. Paulsen, "The effects of internal refractive index variation in near-infrared optical tomography: a finite element modelling approach," Phys. Med. Biol. **48**, 2713–2727 (2003).
11. M. Schweiger and S. R. Arridge, "The finite-element method for the propagation of light in scattering media: frequency domain case," Med. Phys. **24**, 895–902 (1997).
12. F. Gao, H. Niu, H. Zhao, and H. Zhang, "The forward and inverse models in time-resolved optical tomography imaging and their finite-element method solutions," Image Vis. Comput. **16**, 703–712 (1998).
13. A. D. Zacharopoulos, S. R. Arridge, O. Dorn, V. Kolehmainen, and J. Sikora, "Three-dimensional reconstruction of shape and piecewise constant region values for optical tomography using spherical harmonic parametrization and a boundary element method," Inverse Probl. **22**, 1509–1532 (2006).
14. S. Srinivasan, B. W. Pogue, C. Carpenter, P. K. Yalavarthy, and K. Paulsen, "A boundary element approach for image-guided near-infrared absorption and scatter estimation," Med. Phys. **34**, 4545–4557 (2007).
15. A. Klose and E. Larsen, "Light transport in biological tissue based on the simplified spherical harmonics equations," J. Comput. Phys. **220**, 441–470 (2006).
16. A. H. Hielscher, R. E. Alcouffe, and R. L. Barbour, "Comparison of finite-difference transport and diffusion calculations for photon migration in homogeneous and heterogeneous tissues," Phys. Med. Biol. **43**, 1285–1302 (1998).
17. E. D. Aydin, C. R. de Oliveira, and A. J. Goddard, "A comparison between transport and diffusion calculations using a finite element-spherical harmonics radiation transport method," Med. Phys. **29**, 2013–2023 (2002).
18. E. D. Aydin, "Three-dimensional photon migration through void-like regions and channels," Appl. Opt. **46**, 8272–8277 (2007).
19. A. H. Hielscher and R. E. Alcouffe, "Discrete-ordinate transport simulations of light propagation in highly forward scattering heterogenous media," in *Advances in Optical Imaging and Photon Migration*, 1998 OSA Technical Digest Series (Optical Society of America, 1998), paper ATuC2.
20. M. Chu, K. Vishwanath, A. D. Klose, and H. Dehghani, "Light transport in biological tissue using three-dimensional frequency-domain simplified spherical harmonics equations," Phys. Med. Biol. **54**, 2493–2509 (2009).
21. M. L. Adams and E. W. Larsen, "Fast iterative methods for discrete ordinates particle transport calculations," Prog. Nucl. Energy **40**, 3–159 (2002).
22. J. K. Fletcher, "A solution of the neutron transport equation using spherical harmonics," J. Phys. A: Math. Gen. **16**, 2827–2835 (1983).
23. K. Kobayashi, H. Oigawa, and H. Yamagata, "The spherical harmonics method for the multigroup transport equation in x-y geometry," Ann. Nucl. Energy **13**, 663–678 (1986).
24. L. D. Montejo, A. D. Klose, and A. H. Hielscher, "Implementation of the equation of radiative transfer on block-structured grids for modeling light propagation in tissue," Biomed. Opt. Express **1**, 861–878 (2010).
25. K. Ren, G. S. Abdoulaev, G. Bal, and A. H. Hielscher, "Algorithm for solving the equation of radiative transfer in the frequency domain," Opt. Lett. **29**, 578–580 (2004).
26. S. Wright, M. Schweiger, and S. Arridge, "Reconstruction in optical tomography using the PN approximations," Meas. Sci. Technol. **18**, 79–86 (2007).
27. E. Aydin, C. de Oliveira, and A. Goddard, "A finite element-spherical harmonics radiation transport model for photon migration in turbid media," J. Quant. Spectrosc. Radiat. Transfer **84**, 247–260 (2004).
28. R. Wells, A. Celler, and R. Harrop, "Analytical calculation of photon distributions in SPECT projections," IEEE Trans. Nucl. Sci. **45**, 3202–3214 (1998).
29. B. F. Hutton, I. Buvat, and F. J. Beekman, "Review and current status of SPECT scatter correction," Phys. Med. Biol. **56**, R85–R112 (2011).
30. M. A. King, S. J. Glick, P. H. Pretorius, R. G. Wells, H. C. Gifford, and M. V. Narayanan, *Emission Tomography: The Fundamentals of PET and SPECT* (Academic, 2004).
31. W.-F. Cheong, S. A. Prahl, and A. J. Welch, "A review of the optical properties of biological tissues," IEEE J. Quantum Electron. **26**, 2166–2185 (1990).
32. V. G. Peters, D. R. Wyman, M. S. Patterson, and G. L. Frank, "Optical properties of normal and diseased human breast tissues in the visible and near infrared," Phys. Med. Biol. **35**, 1317–1334 (1990).
33. P. Gonzalez-Rodriguez and A. D. Kim, "Comparison of light scattering models for diffuse optical tomography," Opt. Express **17**, 8756–8774 (2009).
34. H. Dehghani, S. Srinivasan, B. W. Pogue, and A. Gibson, "Numerical modelling and image reconstruction in diffuse optical tomography," Phil. Trans. R. Soc. A **367**, 3073–3093 (2009).
35. H. Dehghani, B. W. Pogue, S. P. Poplack, and K. D. Paulsen, "Multiwavelength three-dimensional near-infrared tomography of the breast: initial simulation, phantom, and clinical results," Appl. Opt. **42**, 135–146 (2003).
36. S. Srinivasan, B. W. Pogue, S. Jiang, H. Dehghani, C. Kogel, S. Soho, J. J. Gibson, T. D. Tosteson, S. P. Poplack, and K. D. Paulsen, "In vivo hemoglobin and water concentrations, oxygen saturation, and scattering estimates from near-infrared breast tomography using spectral reconstruction," Acad. Radiol. **13**, 195–202 (2006).
37. T. Austin, A. P. Gibson, G. Branco, R. M. Yusof, S. R. Arridge, J. H. Meek, J. S. Wyatt, D. T. Delpy, and J. C. Hebden, "Three dimensional optical imaging of blood volume and oxygenation in the neonatal brain," Neuroimage **31**, 1426–1433 (2006).
38. B. W. Zeff, B. R. White, H. Dehghani, B. L. Schlaggar, and J. P. Culver, "Retinotopic mapping of adult human visual cortex with high-density diffuse optical tomography," Proc. Natl. Acad. Sci. USA **104**, 12169–12174 (2007).
39. A. H. Hielscher, A. D. Klose, A. K. Scheel, B. Moa-Anderson, M. Backhaus, U. Netz, and J. Beuthan, "Sagittal laser optical tomography for imaging of rheumatoid finger joints," Phys. Med. Biol. **49**, 1147–1163 (2004).
40. A. H. Hielscher, "Optical tomographic imaging of small animals," Curr. Opin. Biotechnol. **16**, 79–88 (2005).
41. B. Gallas and H. H. Barrett, "Modeling all orders of scatter in nuclear medicine," in *IEEE Nuclear Science Symposium*, Vol. 3 (IEEE, 1998), pp. 1964–1968.
42. H. H. Barrett, B. Gallas, E. Clarkson, and A. Clough, *Computational Radiology and Imaging: Therapy and Diagnostics* (Springer, 1999), pp. 71–100.
43. M. Kim, G. Skofronick-Jackson, and J. Weinman, "Intercomparison of millimeter-wave radiative transfer models," IEEE Trans. Geosci. Remote Sens. **42**, 1882–1890 (2004).
44. T. Deutschmann, S. Beirle, U. Frie, M. Grzegorski, C. Kern, L. Kritten, U. Platt, C. Prados-Roman, J. Pukite, T. Wagner,

B. Werner, and K. Pfeilsticker, "The Monte Carlo atmospheric radiative transfer model McArtim: Introduction and validation of Jacobians and 3D features," J. Quant. Spectrosc. Radiat. Transfer **112**, 1119–1137 (2011).

45. Z. Wang, M. Yang, and G. Qin, "Neumann series solution to a neutron transport equation of slab geometry," J. Syst. Sci. Complexity **6**, 13–17 (1993).

46. L. G. Henyey and J. L. Greenstein, "Diffuse radiation in the galaxy," Astrophys. J. **93**, 70–83 (1941).

47. E. W. Hobson, *The Theory of Spherical and Ellipsoidal Harmonics* (Chelsea, 1955).

48. G. Arfken and H. Weber, *Mathematical Methods for Physicists*, Vol. 3 (Academic, 2005).

49. L. Wang, S. L. Jacques, and L. Zheng, "MCML–Monte Carlo modeling of light transport in multi-layered tissues," Comput. Methods Programs Biomed. **47**, 131–146 (1995).

50. J. C. Chai, H. S. Lee, and S. V. Patankar, "Finite volume method for radiation heat transfer," J. Thermophys. Heat Transf. **8**, 419–425 (1994).

51. M. Schweiger, S. R. Arridge, M. Hiraoka, and D. T. Delpy, "The finite element method for the propagation of light in scattering media: boundary and source conditions," Med. Phys. **22**, 1779–1792 (1995).

52. T. Tarvainen, M. Vauhkonen, V. Kolehmainen, and J. P. Kaipio, "Hybrid radiative-transfer-diffusion model for optical tomography," Appl. Opt. **44**, 876–886 (2005).

53. T. Spott and L. O. Svaasand, "Collimated light sources in the diffusion approximation," Appl. Opt. **39**, 6453–6465 (2000).

54. A. K. Jha, M. A. Kupinski, H. H. Barrett, E. Clarkson, and J. H. Hartman, "A three-dimensional Neumann-series approach to model light transport in non-uniform media," J. Opt. Soc. Am. A (to be published).